Structural and spin-glass properties of single crystal J_{eff} = ½ pyrochlore antiferromagnet $NaCdCo_2F_7$: correlating T_f with magnetic-bond-disorder

Physica Scripta

PAPER

Structural and spin-glass properties of single crystal J_{eff} = ½ pyrochlore antiferromagnet $NaCdCo_2F_7$: correlating T_f with magnetic-bond-disorder

A Kancko[1], G Giester[2] and R H Colman[1,*]

[1] Charles University, Faculty of Mathematics and Physics, Department of Condensed Matter Physics, Ke Karlovu 5, 121 16 Prague 2, Czech Republic
[2] Institut für Mineralogie und Kristallographie, Universtät Wien, Austria
[*] Author to whom any correspondence should be addressed.

E-mail: ross.colman@mag.mff.cuni.cz

Keywords: pyrochlore, cobalt, frustrated magnetism, spin-glass, structural disorder

OPEN ACCESS

RECEIVED
10 March 2023

REVISED
12 June 2023

ACCEPTED FOR PUBLICATION
15 June 2023

PUBLISHED
29 June 2023

Abstract

Weak bond disorder disrupts the expected spin-liquid ground-state of the ideal $S = 1/2$ Heisenberg pyrochlore antiferromagnet. Here we introduce a single crystal study of the structural and magnetic properties of the bond-disordered pyrochlore $NaCdCo_2F_7$. The magnetic susceptibility appears isotropic, with a large negative Curie-Weiss temperature ($\theta_{CW} = -108(1)$ K), however no magnetic order is observed on cooling until a spin-glass transition at $T_f = 4.0$ K. AC-susceptibility measurements show a frequency-dependent shift of the associated cusp in χ' at T_f, that can be fitted well by the empirical Vogel-Fulcher law. The magnetic moment of $\mu_{eff} = 5.4(1)\ \mu_B/Co^{2+}$ indicates a significant orbital contribution and heat capacity measurements show that down to 1.8 K, well below T_f, only $S_{mag} \sim 2/3$ Rln(2) of the magnetic entropy is recovered, suggestive of residual continued dynamics. Structural and magnetism comparisons are made with the other known members of the $NaA''Co_2F_7$ family ($A'' = Ca^{2+}, Sr^{2+}$), confirming the expected relationship between spin-glass freezing temperature, and extent of magnetic bond disorder brought about by the size mismatch between A-site ions.

Introduction

The properties of $S = ½$ Heisenberg pyrochlore antiferromagnet remain hotly contentious as it is a notoriously difficult system to model theoretically using current methods. The ground-state predictions are strongly method-dependent and range from dimer singlet phases [1–3], spin-liquids with short-range correlations [4], as well as chiral spin liquids [5, 6].

To complement and confirm the theories, model materials must be found and studied, as close as possible to the ideal case. Pyrochlore lattices of magnetic ions exist in a number of real materials, most commonly in both the spinel, AB_2O_4, and pyrochlore, $A_2B_2O_7$, oxides [7–11]. Structural stability and charge balancing constraints of the pyrochlore oxides mean that the magnetic ions that are most commonly hosted are rare-earth A^{3+} ions. Several rare-earth pyrochlore oxides have been proposed as having spin-liquid ground-states [12–14], although the contracted nature of the 4*f* orbitals means that magnetic exchange energies are typically low (typically 0.1–1 meV), and very low temperatures are required to study the spin-liquid-state properties.

A relatively less studied family is that of the pyrochlore fluorides $A'A''M_2F_7$, where: A' is a monovalent cation, A'' is a divalent cation, and M is a divalent 3*d* transition metal ion. The magnetic properties of several members of this group (with $A' = Na^+$, $A'' = Ca^{2+}$ or Sr^{2+}, and $M = Co^{2+}$, Ni^{2+}, Fe^{2+} and Mn^{2+}) have already been reported, with only the Co and Ni members extensively studied [15–18]. The more spatially extensive 3*d* orbitals result in greater orbital overlap and significantly stronger magnetic exchange interactions (typically 10–100 meV), evidenced by the relatively large Curie-Weiss temperatures so far observed ($|\theta_{CW}| \sim 70$–140 K).

The noteworthy deviation from ideality in these fluoride pyrochlores is the necessity for mixed ion occupancy on the A-site (A'^{+} and A''^{2+}), due to the charge balancing requirement for an average $A^{1.5+}$ oxidation state. No structural ordering of these A-site ions has been found, which leads to small local-structure deviations from the average structure because of ion size mismatches between A' and A". These local structural deviations transcribe onto the magnetic interactions too, introducing magnetic exchange disorder that eventually results in spin-glass freezing rather than the fully-dynamic spin-liquid state predicted by some models in an ideal $S = 1/2$ Heisenberg pyrochlore antiferromagnet [19, 20].

Despite the apparent spin-glass transition at 4 K, the $S = 1$ $NaCaNi_2F_7$ shows persistent spin dynamics down below 80 mK and a continuum of excitations observed by inelastic neutron scattering suggests a large manifold of low-energy states [21, 22]. A similar picture is found in both $J_{\rm eff} = ½$ $NaCaCo_2F_7$ and $NaSrCo_2F_7$, where a short-range-ordered state is selected from a continuous manifold of low-energy states and frozen in at $T_f = 2.4$ K and 3.0 K, respectively [23, 24]. Comparison of Monte Carlo simulations with NMR data confirms the importance of quantum fluctuations and single-ion anisotropy in driving the low-temperature properties of these systems [25].

In this paper our single crystal study introduces a new, isostructural and isoelectronic member of this $J_{\rm eff} = ½$ pyrochlore family: $NaCdCo_2F_7$. We present the synthesis and structural analysis, comparing with the previously studied Co^{2+} pyrochlore antiferromagnets. Magnetic and thermodynamic investigations characterise the spin-freezing transition, and we consider the structure-property relationships that drive the spin-freezing transition temperature across this series.

Experimental methods

Single crystals of $NaCdCo_2F_7$ were grown using a laser floating zone furnace (Crystal Systems Corp. FZ-LD-5–200W-II-VPO-PC). Dry elemental fluorides were weighed out and ground in a glove-box due to their hygroscopic nature. The mixture was then filled into a hollow graphite tubular crucible and melted in the laser furnace under an 8 bar atmosphere of argon, at ~1000 °C (using infrared pyrometry and assuming an emissivity of 0.85 for graphite), to form a polycrystalline precursor rod. After cooling, the rod was extracted from the graphite crucible and re-mounted within the furnace for standard floating-zone growth using platinum wire. The growth was again performed under a dynamic flow of argon atmosphere (0.25 l min^{-1}) at high pressure (8 bar) to minimize evaporation, with melting point ~750 °C (assuming an emissivity of 0.72). The red oligocrystalline ingot was broken into smaller pieces, many of which were single grain fragments. A small selection of the grains was crushed into a fine powder and analysed by Powder x-ray Diffraction (PXRD) using a Bruker D8 Advance diffractometer with CuKα1 and CuKα2 radiation ($\lambda = 1.5418$ Å), and a structural refinement was performed using Topas Academic V6 [26]. Neighbouring pieces were used for both single crystal property measurements and single crystal x-ray diffraction analysis. Single crystal diffraction was performed at 200 K using a Bruker Kappa X8 APEX diffractometer equipped with a CCD detector and Incoatec Microfocus Source IμS (30 W, multilayer mirror, Mo$K\alpha$). All atomic structure figures were prepared using Vesta 3 [27]. X-ray fluorescence (XRF) spectroscopy was performed using an EDAX AMETEK ORBIS-PC spectrometer equipped with a Rh anode tube ($E_{K\alpha} = 20.216$ keV) and Apollo XRF ML-50 EDS detector with polycapillary focusing optics (~184 × 69 μm^2 spot size). Orienting of the crystals for magnetic and physical property measurements was carried out using a PhotoScience Laue diffractometer. Temperature and field dependent DC susceptibility measurements on the oriented crystals were performed in a Quantum Design Magnetic Property Measurement System (model MPMS-XL 7T), using the reciprocating sample option (RSO). Temperature and frequency dependent AC susceptibility measurements were made using the ACMS II option in a Quantum Design Physical Property Measurement System (PPMS). Heat capacity was measured via the heat relaxation method also in the PPMS, with the addition of a ^{3}He low-temperature insert, using a non-magnetic sapphire stage and Apiezon-N grease for mounting the crystal. For subtraction of the lattice contribution to specific heat, a sample of the non-magnetic analogue $NaCdZn_2F_7$ was also prepared using the synthesis techniques described above for $NaCdCo_2F_7$.

Results

Structure

The single crystal reflections could be indexed by space-group Fd-3m with cell parameter $a = 10.3488(5)$ Å. The solved structure, summarised in table 1, is isostructural to that of $NaSrCo_2F_7$ [16], $NaCaCo_2F_7$ [15], and the other recently studied pyrochlore fluorides shown in figure 1(a) [17, 18]. As with these previous examples, no superstructure reflections were seen, indicating no ordering of Na and Cd on the pyrochlore (16d) A-site. The Cd:Co ratio was confirmed on several of the single crystal pieces by XRF spectroscopy to be 1:2.0(1), and was

Table 1. Single crystal structure solution.

Space group: $Fd-3m$ (227, origin 2)				$a = 10.3488(5)$Å			$V = 1108.3(3)$ Å^3		$Z = 8$		
Radiation: Mo Kα				$T = 200$ K			*Reflections collected/unique: 17497/179*		*Parameters: 11*		
Goodness of fit: 1.274				Final R indices: $R = 1.55\%$, $wR = 3.95\%$			*Largest difference: Peaks Holes*		*0.535 e Å^{-3}*−0.542 e Å^{-3}		
Atom	Site	x/a	y/a	z/a	Occ.	U_{11} /(Å$^2 \times 10^{-3}$)	U_{22}	U_{33}	U_{23}	U_{13}	U_{12}
Na	16*d*	0.5	0.5	0.5	0.5	16.02(14)	16.02(14)	16.02(14)	−2.93(6)	−2.93(6)	−2.93(6)
Cd	16*d*	0.5	0.5	0.5	0.5	16.02(14)	16.02(14)	16.02(14)	−2.93(6)	−2.93(6)	−2.93(6)
Co	16*c*	0	0	0	1	8.31(13)	8.31(13)	8.31(13)	−0.33(5)	−0.33(5)	−0.33(5)
F(1)	8*b*	0.375	0.375	0.375	1	17.0(5)	17.0(5)	17.0(5)	0	0	0
F(2)	48*f*	0.33415(15)	0.125	0.125	1	25.1(7)	20.2(4)	20.2(4)	10.5(5)	0	0

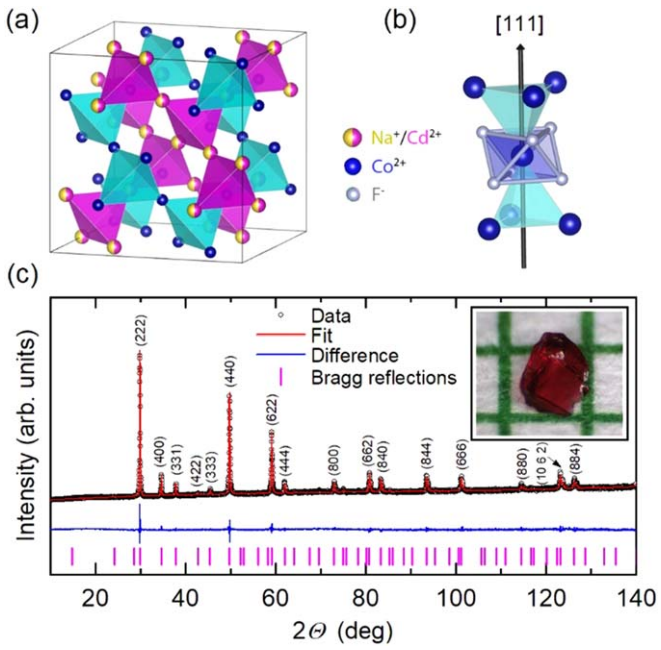

Figure 1. (a) Crystal structure of $NaCdCo_2F_7$, highlighting the pyrochlore lattice of $J_{eff} = ½$ Co^{2+} ions, with F^- ions left off for clarity, and the intertwined pyrochlore lattice of the mixed-occupancy Na^+/Cd^{2+} *A*-site. (b) The local octahedral coordination environment of the CoF_6 unit, superimposed on vertex-sharing tetrahedral magnetic exchange lattice. (c) Powder diffraction data of crushed $NaCdCo_2F_7$ crystal, collected at 300 K. Miller indices are indicated. Rietveld refinement using the pyrochlore structure finds $a = 10.3638(2)$ Å with a goodness-of-fit, $\chi^2 = 1.99$.

constrained as this ideal stoichiometry for the reported structure below. However, the single crystal refinement showed a preference for a slightly increased electron density on the Co (16*c*) site. We attempted to model this by joint Co:Cd occupation which lead to a ratio of 0.959(2):0.041(2), respectively, a final composition of $NaCd_{1.08}Co_{1.92}F_7$ with a drop in *R*-factor from 1.55 to 1.19%, compared to the ideal stoichiometry case. To further confirm the single crystal solution is representative of the bulk, powder x-ray diffraction was collected on a specimen of powder after crushing several grains. Figure 1(c) shows the results of Rietveld refinement using the ideal stoichiometry pyrochlore structure solution.

Magnetic susceptibility

Temperature-dependent DC magnetic susceptibility measurements (determined as $\chi = M/H$ in a constant field $H = 2000$ Oe), with the field applied along the [100], [110] and [111] crystallographic directions of $NaCdCo_2F_7$, are shown in figure 2(a). In all calculations, the ideal stoichiometry, $NaCdCo_2F_7$, was used. The data in all three high symmetry directions appear Curie-Weiss-like and overlay, suggesting an isotropic magnetic behaviour $NaCdCo_2F_7$. The inverse susceptibility $\chi^{-1}(T)$ data with H ‖ [111] (figure 2(b)) were used for a Curie-Weiss fit in the temperature range of 100−350 K, in the standard form of $\chi = C/(T\text{-}\Theta_{CW})$, where $C = N_A\mu_{eff}^2/3k_B$ is the Curie constant, N_A is Avogadro's number, μ_{eff} is the effective magnetic moment, k_B is Boltzmann's constant and Θ_{CW} is the Curie-Weiss temperature. The bottom right inset shows a linear dependence of magnetisation versus field (at $T = 2$ K) up to $\mu_0 H = 7$ T, justifying our calculation of susceptibility as M/H at 2000 Oe. The Curie-Weiss fit of the temperature-dependent susceptibility data yields a large negative Curie-Weiss temperature (a mean-field measure of the interaction strength) of approximately $\Theta_{CW} \approx -108(1)$ K, confirming dominant antiferromagnetic interactions in $NaCdCo_2F_7$. The effective moment per cobalt was extracted as $\mu_{eff} \approx 5.4(1)$ μ_B, which is significantly larger than the expected $S = 3/2$ Co^{2+} spin-only value (3.87 μ_B), and is approaching the $J = 9/2$ total angular momentum value (6.63 μ_B), as was seen previously in the other isostructural analogues [15, 16].

A cusp at $T = 4.0$ K seen in the inset of figure 2(a), concomitant with bifurcation of the ZFC and FC data indicates a magnetic transition with history dependence, suggestive of either magnetic ordering or spin freezing into a disordered state – a spin glass.

To further probe the observed 4 K cusp in DC measurements, AC susceptibility measurements were performed. The low temperature region shows again a cusp in χ', with a weak but well defined frequency-dependent shift, indicative of a spin-glass ground-state (figure 3 inset). The extracted dimensionless Mydosh parameter follows the relative shift of T_f per decade of frequency, $K = \Delta T_f/(T_f \Delta \log \nu) = 0.010(1)$ [28]. This value is smaller than those expected for superparamagnetic or cluster-glass states, is in line with those seen

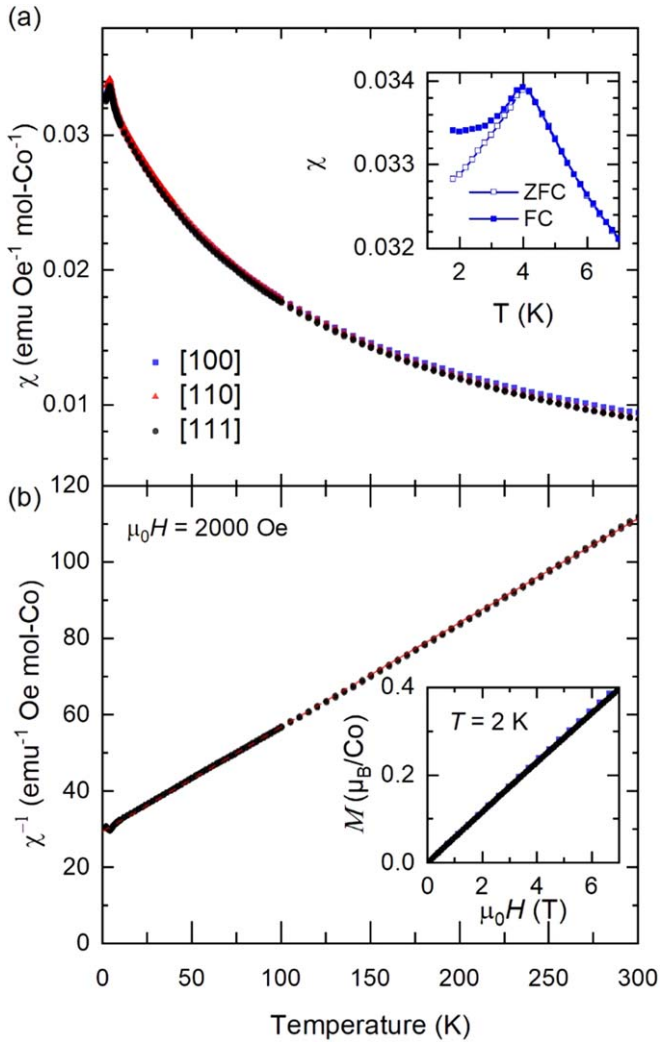

Figure 2. (a) Temperature-dependent DC-magnetic-susceptibility for $NaCdCo_2F_7$ along significant crystallographic directions at $\mu_0 H = 2000$ Oe. The inset highlights a low-temperature cusp. (b) Inverse susceptibility for $H \| [111]$, with Curie-Weiss fit (red line). The inset shows $M(H)$ at 2 K, indicating a linear dependence of the magnetic response of all crystallographic directions up to $\mu_0 H = 7$ T.

in the isostructural analogues [15, 16], and is typical of other insulating spin-glass systems [29, 30]. Additional inferences about the properties of the spin-glass are typically extracted by fitting the frequency-dependent shift to the Vogel-Fulcher law, which takes into account the interactions of clusters of spins during the dynamic freezing process [28]. The Vogel-Fulcher law expects a frequency-dependence of $T_f = T_0 - \frac{E_a}{k_B} \frac{1}{\ln(\tau_0 \nu)}$, where T_0 is the ideal glass temperature, E_a is the activation energy of the transition and τ_0 is the intrinsic relaxation time. Since we are fitting a restricted frequency range, free fitting of all parameters is not stable and instead τ_0 is typically fixed to a reasonable value of 10^{-12} s. These parameters can be extracted from a fit of T_f versus $-1/\ln(\tau_0 \nu)$, resulting in $E_a = 6.6(6).10^{-4}$ eV and $T_0 = 3.7(1)$ K, shown in figure 3.

Specific heat

The temperature dependence of the specific heat is shown in figure 4(a). The lattice contribution was subtracted using an isostructural non-magnetic analogue $NaCdZn_2F_7$ [31]. With no contribution to the total heat capacity from conduction electrons due to the insulating nature of $NaCdCo_2F_7$, the resulting magnetic contribution to the specific heat, C_{mag}, can be approximated as

$$C_{mag} = C_p - C_{lattice} \approx C_{p[NaCdCo_2F_7]} - C_{p[NaCdZn_2F_7]}.$$

A significant magnetic contribution can be seen in figure 4(b) at low temperatures, starting on cooling below ~40 K with a maximum in C_{mag}/T versus T (figure 4 (a) inset) at 4.0 K. The high temperature (>100 K) apparent additional contribution to C_{mag}/T is likely due to transitions to the first Kramers' doublet excited state, found to be 28.05(2) and 29.31(2) meV in isostructural $NaCaCo_2F_7$ and NaSrCo2F7, respectively [24]. This high-

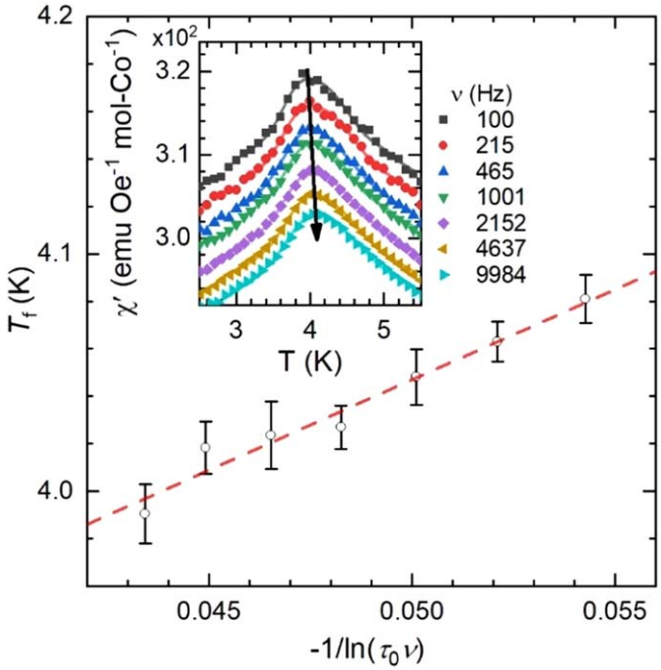

Figure 3. AC-susceptibility of $NaCdCo_2F_7$, showing the frequency dependence of a peak in χ' as a function of both temperature and frequency, ν, in the inset. With the frequency dependence of the freezing temperature, T_f, fitted according to the Vogel-Fulcher law in the main panel.

temperature heat capacity peak can be fitted reasonably well by a simple 2-level Schottky anomaly, in the range $50 < T(\mathrm{K}) < 250$, using

$$C_{Schottky} = R\left(\frac{\Delta}{T}\right)^2 \frac{e^{\Delta/T}}{(1+e^{\Delta/T})^2},$$

where R is the ideal gas constant and Δ is the magnitude of the energy gap. The resulting fit (figure 4 (b) inset) gives an energy to the first single ion excited state of 33.9(5) meV, well in line with those previously seen, although other spectroscopic techniques would be needed to better refine this value.

Below T_f the magnetic contribution to specific heat shows a power-law decay (figure 4(b)). The $T < T_f$ data was fitted to a simple power function, $C_{mag} = AT^{\alpha}$, resulting in values of $A = 0.115(10)$ J mol-Co^{-1} K$^{-1-\alpha}$ and exponent $\alpha = 1.744(7)$. A linear dependence of $C_{mag}(T)$ is expected below T_f according to most canonical spin-glass models and has been observed in the metallic spin glasses [28, 32]. Power-law behaviour has been theoretically predicted in positionally disordered $S = 1/2$ antiferromagnetic models due to the temperature (variable range interaction strength) dependent formation of spin-singlet dimers, within a matrix of paramagnetic spins [33]. This scaling behaviour expects values of $\alpha < 1$, and has successfully been applied to several $S = ½$ frustrated spin systems [34, 35], but does not explain the larger $\alpha = 1.744(7)$ we observe. An α of 2 was found in the $S = 3/2$ kagome lattice compound $SrCr_9Ga_{12}O_{19}$ [36]. This value of $\alpha \sim 2$ has been observed in several models that are explained by the heat capacity being dominated by low-lying singlet states [37]. On the pyrochlore lattice, an $\alpha \sim 2$ has been observed in several experimental systems, such as $NaCaNi_2F_7$ and $Y_2Mo_2O_7$ [21, 38]. Theoretical calculations have not yet converged on a unified behaviour of specific heat but recent models also suggest power law behaviour with α likely in the vicinity of 2 [39].

The magnetic entropy, $S_{mag}(T)$, is shown in figure 4(c), and is consistent with the assignment of an $J_{eff} = 1/2$ magnetic ground-state, approaching but noticeably short of even a value of Rln(2). This is far below the value expected for an orbitally quenched spin-only $S = 3/2$ state value of $S_{mag} = \mathrm{Rln}(4)$. The suppression of the peak with increasing applied field, seen in the inset of figure 4(a), is typical of antiferromagnetic spin-glass systems [32].

Discussion

First we must consider the structure of $NaCdCo_2F_7$, and compare its details with those of its isoelectronic analogues $NaSrCo_2F_7$ and $NaCaCo_2F_7$. The structure matches that of the other pyrochlore fluorides, with a lattice parameter slightly less than empirical predictions using the A and B-site ion sizes ($a_{exp} = 10.3638(2)$ Å,

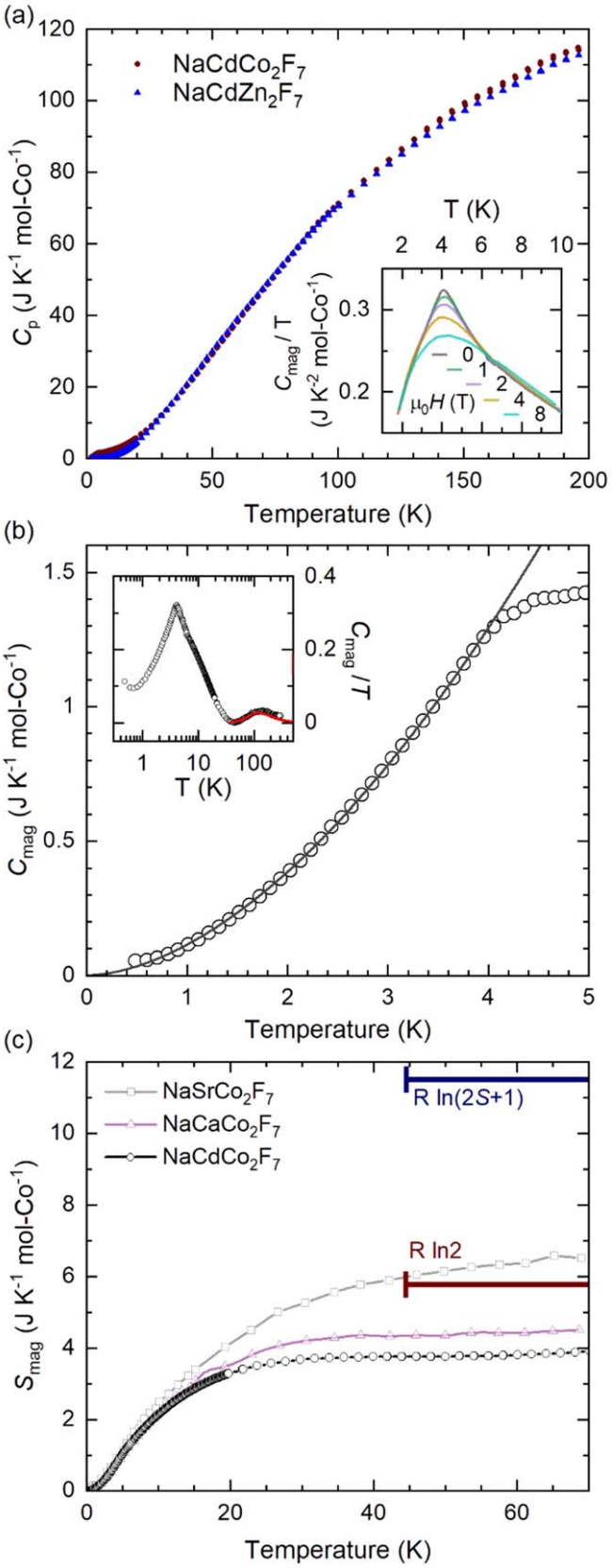

Figure 4. (a) Temperature dependent heat capacity of $NaCdCo_2F_7$ and non-magnetic analogue $NaCdZn_2F_7$ in zero field. Inset shows a zoom of the low temperature region of the magnetic component, C_{mag}/T, for $NaCdCo_2F_7$ with multiple applied fields ($H \parallel [100]$). (b) shows the power-law decay of C_{mag} below T_f, with line showing the fit to $C_{mag} \propto T^{\alpha}$, with $\alpha = 1.744(7)$. The inset shows the expanded temperature dependence of C_{mag}/T on a logarithmic scale, with the red line showing a 2-level system Schottky fit, described in the text. (c) The change in magnetic entropy, S_{mag}, saturating at ~2/3 Rln(2), with comparisons to previously published data for related $NaSrCo_2F_7$ and $NaCaCo_2F_7$, extracted from [16] and [15], respectively.

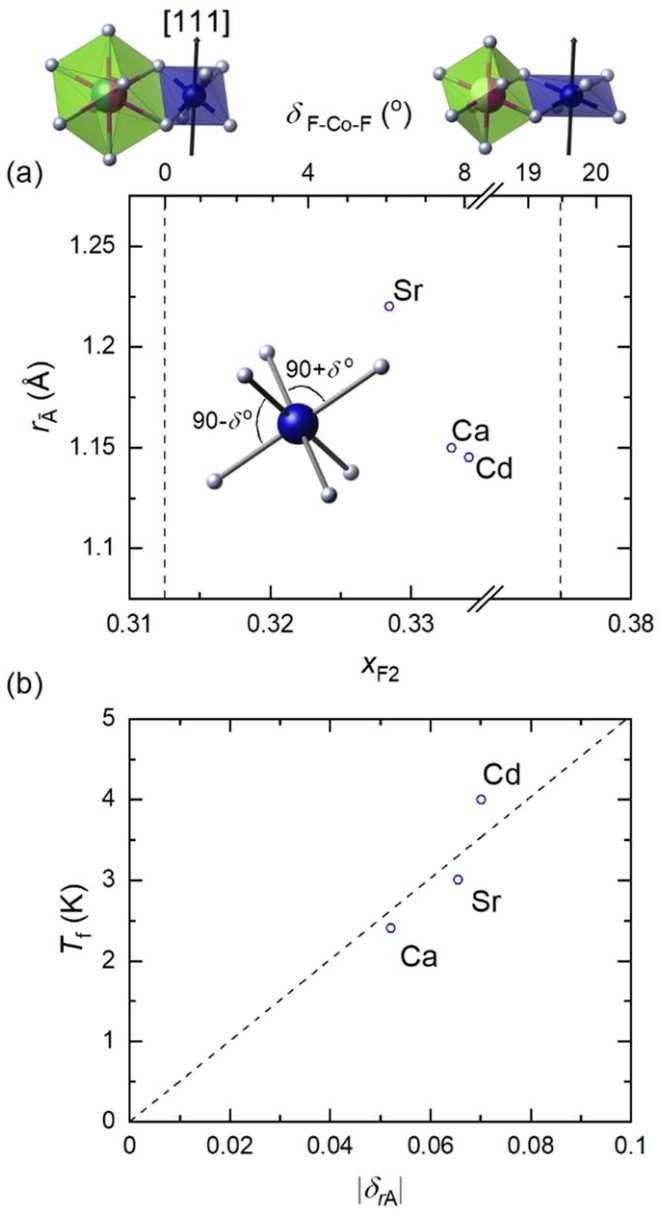

Figure 5. Comparison of the level of distortion away from a regular octahedron of the CoF_6 triangular antiprisms in the Na*A*″*Co*$_2$*F*$_7$ *series, with* A″ = Sr^{2+}, Ca^{2+} and Cd^{2+}. (b) Correlation between *A*-site ion size discrepancy, $|\delta_{rA}|$, and the spin-glass freezing temperature, T_f.

$a_{pred} = 10.371$ Å, for experimental and predicted, respectively) [40]. It is worth noting that several other Cd-containing pyrochlores were omitted during creation of the empirical model as they were also systematically lower than those predicted.

Full site disorder of the *A*-site is still maintained on mixing of $A'' = Cd^{2+}$ with $A' = Na^{+}$. Using the VIII coordination Shannon ionic radii for each ion [41], the ion size discrepancy, $\delta_{rA} = 2(r_{A'} - r_{A''})/(r_{A'} + r_{A''})$ is −6.6%, 5.2%, and 7.0% for Na^{+} with Sr^{2+}, Ca^{2+} and Cd^{2+}, respectively. Whilst the *A*-site is not directly involved in magnetic exchange, variation of the *A*-site ions can introduce subtle changes to the structure that indirectly affect the magnetic properties discussed in the following paragraphs.

The pyrochlore structure has very limited allowed variation as only one crystallographic parameter is not constrained by symmetry—the F2 (48*f*) site *x*-coordinate, x_{F2}. All other atoms are fully constrained to high-symmetry positions. Two easy to describe extremes for the x_{F2}-coordinate exist, illustrated in figure 5(a), resulting in a situation ranging from: an ideal octahedral coordination of the BF_6 group, with a highly distorted AF_8 polyhedron, at $x_{F2} = 0.3125$ on the left; to a trigonally compressed BF_6 triangular antiprism, with an ideal cube AF_8 unit, at $x_{F2} = 0.375$ on the right. In $NaCdCo_2F_7$ $x_{F2} = 0.33415(15)$, which results in a variation of the F-Co-F bond angles of $\pm\delta_{F\text{-}Co\text{-}F} = 8.12(5)°$ away from the ideal 90° due to the trigonal compression along the [111] axis. The x_{F2} coordinate, and subsequently the extent of trigonal compression of the CoF_6 octahedron, is

seen to correlate with the average *A*-site ionic radii, showing increasing trigonal compression as the ionic radius decreases from $A'' = Sr^{2+}$, towards Cd^{2+}.

When a Co^{2+} ($3d^7$) ion is in an octahedral crystal field, the degenerate (^4F) ground state is first split into $^4A_2$ (highest), $^4T_2$, and $^4T_1$ (lowest) terms. With a trigonal distortion and spin–orbit coupling, this $^4T_1$ term can further split into six Kramers doublets, with an effective $J_{eff} = 1/2$ doublet as the ground state [42, 43]. The low-magnetic entropy associated with the spin-freezing transition (<Rln(2)) seems to confirm this spin–orbit-coupled ground-state, in agreement with the previous spectroscopic studies of the isostructural family members [24].

Increasing the trigonal distortion of the Co^{2+} octahedron has previously been shown to increase the *g*-factor anisotropy [44]. A similar situation has been proposed in the rare-earth iridate pyrochlores $A_2Ir_2O_7$, where *chemical pressure* through rare-earth substitution on the *A*-site leads to increased tetragonal distortion that increases spin-anisotropy and promotes a magnetically ordered state [45–47]. Although the Heisenberg $S = 1/2$ pyrochlore ground-state is predicted to be a quantum spin-liquid [48], increasing single-ion anisotropy to either XY-planar or uniaxial Ising has the potential to drive the system to order [49, 50]. In our case of $NaCdCo_2F_7$, the extent of magnetic anisotropy is not yet established, but our low-field magnetisation measurements, where χ(T) of [100], [110], and [111] overlay, suggest isotropic magnetism. Similarly, both low-field and high-field (up to $\mu_0 H = 60$ T) magnetisation measurements on $NaCaCo_2F_7$ also overlay perfectly, initially suggesting low-to-zero magnetocrystalline anisotropy, confirmed with electron spin resonance spectroscopy measurements that give an isotropic *g*-factor of ~2 [51]. These result are, however, inconsistent with inelastic neutron scattering data that are interpreted with a model showing short-range XY-like correlations with a g-tensor anisotropy of $g_{xy}/g_z \sim 3$ in $NaCaCo_2F_7$ [23, 24, 52]. These conflicting conclusions prompt further spectroscopic studies of this and other members of the transition metal pyrochlores. The increasing distortion of the CoF_6 octahedron, seen in figure 5(a), suggests that $NaCdCo_2F_7$ is likely to have the largest anisotropy (most likely XY-like) of the so-far investigated members of this family. The presence of Cd in the compound significantly complicates the use of neutrons to investigate this, however.

The inherent structural disorder due to mixed *A*-site occupancy in the $A'A''M_2F_7$ pyrochlores is held responsible for the spin-glass ground-state found in all members so far. Monte Carlo simulations of weak magnetic-exchange disorder, Δ, in the pyrochlore Heisenberg antiferromagnet predict a spin-glass ground-state, with $T_f \propto \Delta$ when $\Delta \ll J$ [19, 20]. The observed increase in T_f across the series of Ca^{2+}, Sr^{2+} to Cd^{2+}, from 2.4 K and 3.0 K to 4.0 K, where *A*-site ion-size mismatch, $|\delta_{rA}|$ increases from 5.2% and 6.6% to 7.0%, respectively, supports this conclusion (figure 5(b). In this scenario we are of course considering the *A*-site ions to be purely spectators here, ignoring any potential additional electronic effects that may occur due to the presence of a filled 3*d*-shell in the case of Cd^{2+} occupying the *A*-site.

The increasing *A*-site disorder is also correlated with both a drop in the Curie-Weiss antiferromagnetic coupling strength from $\theta_{CW} = -140$ K in $NaCaCo_2F_7$ to -108 K in $NaCdCo_2F_7$; and the extracted effective moment from 6.1 to 5.4 μ_B/Co, respectively, in the Curie-Weiss fits. The reduction in Curie-Weiss temperature in concert with the increase in spin-freezing temperature results in a reduction in the Ramirez frustration index, $f = |\theta_{CW}|/T_f$, from 58 where $A'' = Ca^{2+}$ to 27 for Cd^{2+}, although any 3-dimensional magnet with $f > 10$ can be considered highly geometrically-frustrated [53].

Conclusions

We have reported the single-crystal growth, structural parameters, thermodynamic and magnetic properties measurements of a new $J_{eff} = ½$ pyrochlore antiferromagnet, $NaCdCo_2F_7$. Despite strong antiferromagnetic interactions no sign of magnetic ordering occurs on cooling, until a spin-freezing transition is observed at $T_f = 4.0$ K, confirmed by AC-susceptibility and specific heat measurements. The low magnetic entropy recovered at the spin-glass transition, $S_{mag} \sim 2/3$ Rln(2), suggests continued dynamics at lower temperatures, as seen in $NaCaNi_2F_7$ [21]. Magnetisation measurements along specific crystallographic directions indicate isotropic magnetism, although conflicting experimental results within this family of materials prompt further spectroscopic investigations. Regrettably, the neutron absorption cross-section of natural Cd will prevent some of the most informative investigations such as direct determination of crystal field parameters [24, 47].

Through comparison to the previously studied isostructural analogues, $NaSrCo_2F_7$ and $NaCaCo_2F_7$, the effects of subtle structural changes can be better understood. Increasing the size variance between randomly distributed *A*-site ions increases the magnetic exchange interaction disorder and pushes the system further from the expected spin-liquid ground-state in an ideal Heisenberg pyrochlore antiferromagnet. The increasing spin-freezing transition temperature is correlated with increasing *A*-site ion-size mismatch. Understanding how much these materials deviate from an ideal $S = 1/2$ Heisenberg pyrochlore antiferromagnetic system will be an

important consideration when comparing this materials' properties to the continuously developing theoretical predictions for the Quantum Pyrochlore Antiferromagnet, a notoriously difficult-to-model system.

Acknowledgments

This work was supported by the Czech Science Foundation (project no. 19-21575Y). The preparation, characterization and measurement of bulk physical properties were performed in MGML (http://mgml.eu/), which was supported within the program of Czech Research Infrastructures (project no. **LM2023065**), as well as the OP VVV project MATFUN (number CZ.02.1.01/0.0/0.0/15_003/0000487). The authors additionally thank Gaël Bastien and Milan Klicpera for useful discussions.

Data availability statement

All data that support the findings of this study are included within the article (and any supplementary files).

ORCID iDs

A Kancko https://orcid.org/0000-0001-5063-195X
R H Colman https://orcid.org/0000-0002-5039-9764

References

[1] Tsunetsugu H 2001 Spin-singlet order in a pyrochlore antiferromagnet *Phys. Rev.* B **65** 024415
[2] Moessner R, Sondhi S L and Goerbig M O 2006 Quantum dimer models and effective hamiltonians on the pyrochlore lattice *Phys. Rev.* B **73** 094430
[3] Hering M, Noculak V, Ferrari F, Iqbal Y and Reuther J 2022 Dimerization tendencies of the pyrochlore heisenberg antiferromagnet: a functional renormalization group perspective *Phys. Rev.* B **105** 054426
[4] Iqbal Y, Müller T, Ghosh P, Gingras M J P, Jeschke H O, Rachel S, Reuther J and Thomale R 2019 Quantum and classical phases of the pyrochlore heisenberg model with competing interactions *Phys. Rev. X* **9** 011005
[5] Kim J H and Han J H 2008 Chiral spin states in the pyrochlore heisenberg magnet: fermionic mean-field theory and variational monte carlo calculations *Phys. Rev.* B **78** 180410
[6] Schneider B, Halimeh J C and Punk M 2022 Projective symmetry group classification of chiral Z2 spin liquids on the pyrochlore lattice: application to the spin- 1/2 XXZ Heisenberg Model *Phys. Rev.* B **105** 125122
[7] Reig-i-Plessis D and Hallas A M 2021 Frustrated magnetism in fluoride and chalcogenide pyrochlore lattice materials *Phys. Rev. Mater.* **5** 030301
[8] Gardner J S, Gingras M J P and Greedan J E 2010 Magnetic pyrochlore oxides *Rev. Mod. Phys.* **82** 53
[9] Klicpera M, Vlášková K and Diviš M 2020 Low-temperature properties of pyrochlore Lu2Ir2O7 *J. Magn. Magn. Mater.* **506** 166793
[10] Vlášková K, Colman R H and Klicpera M 2021 Synthesis of Er2Ir2O7 pyrochlore iridate by solid-state-reaction and CsCl flux method *Mater. Chem. Phys.* **258** 123868
[11] Vlášková K, Proschek P, Pospíšil J and Klicpera M 2020 Low-temperature study of an Er2Ti2O7 single crystal synthesized by floating zone technique and simplified feed rod preparation route *J. Cryst. Growth* **546** 125783
[12] Sibille R *et al* 2017 Coulomb spin liquid in anion-disordered pyrochlore Tb2Hf2O7 *Nat. Commun.* **8** 892
[13] Sibille R, Lhotel E, Pomjakushin V, Baines C, Fennell T and Kenzelmann M 2015 Candidate quantum spin liquid in the Ce3+ pyrochlore stannate Ce2Sn2O7 *Phys. Rev. Lett.* **115** 097202
[14] Gao B *et al* 2019 Experimental signatures of a three-dimensional quantum spin liquid in effective spin-1/2 Ce2Zr2O7 pyrochlore *Nat. Phys.* **15** 1052
[15] Krizan J W and Cava R J 2014 NaCaCo2F7: A single-crystal high-temperature pyrochlore antiferromagnet *Phys. Rev.* B **89** 214401
[16] Krizan J W and Cava R J 2015 NaSrCo2F7, a Co2+ pyrochlore antiferromagnet *J. Phys. Condens. Matter* **27** 296002
[17] Krizan J W and Cava R J 2015 NaCaNi2 F7: a frustrated high-temperature pyrochlore antiferromagnet with S=1 Ni2 *Phys. Rev.* B **92** 014406
[18] Sanders M B, Krizan J W, Plumb K W, McQueen T M and Cava R J 2017 NaSrMn2F7, NaCaFe2F7, and NaSrFe2F7: novel single crystal pyrochlore antiferromagnets *J. Phys. Condens. Matter* **29** 045801
[19] Saunders T E and Chalker J T 2007 Spin freezing in geometrically frustrated antiferromagnets with weak disorder *Phys. Rev. Lett.* **98** 157201
[20] Andreanov A, Chalker J T, Saunders T E and Sherrington D 2010 Spin-glass transition in geometrically frustrated antiferromagnets with weak disorder *Phys. Rev.* B **81** 014406
[21] Plumb K W, Changlani H J, Scheie A, Zhang S, Krizan J W, Rodriguez-Rivera J A, Qiu Y, Winn B, Cava R J and Broholm C L 2019 Continuum of quantum fluctuations in a three-dimensional S = 1 Heisenberg magnet *Nat. Phys.* **15** 54
[22] Cai Y *et al* 2018 Musr study of spin freezing and persistent spin dynamics in NaCaNi2F7 *J. Phys. Condens. Matter* **30** 385802
[23] Ross K A, Krizan J W, Rodriguez-Rivera J A, Cava R J and Broholm C L 2016 Static and dynamic XY -like short-range order in a frustrated magnet with exchange disorder *Phys. Rev.* B **93** 014433
[24] Ross K A, Brown J M, Cava R J, Krizan J W, Nagler S E, Rodriguez-Rivera J A and Stone M B 2017 Single-ion properties of the Seff = 12 XY antiferromagnetic pyrochlores NaA′Co2F7 (A′ = Ca2+, Sr2+) *Phys. Rev.* B **95** 144414
[25] Sarkar R, Krizan J W, Brückner F, Andrade E C, Rachel S, Vojta M, Cava R J and Klauss H-H 2017 Spin freezing in the disordered pyrochlore magnet NaCaCo2F7 : NMR studies and monte carlo simulations *Phys. Rev.* B **96** 235117
[26] Coelho A 2018 TOPAS and TOPAS-Academic: an optimization program integrating computer algebra and crystallographic objects written in C++ *J. Appl. Crystallogr.* **51** 210–8

[27] Momma K and Izumi F 2011 and IUCr VESTA 3 for three-dimensional visualization of crystal, volumetric and morphology data *J. Appl. Crystallogr.* **44** 1272
[28] Mydosh J A 1993 *Spin Glasses : an Experimental Introduction* (London: Taylor & Francis)
[29] Vlášková K, Colman R H, Proschek P, Čapek J and Klicpera M 2019 Evidence for spin-glass ground state in fluorite-defect Er2Zr2O7 single crystals *Phys. Rev.* B **100** 214405
[30] Colman R H and Mclaughlin A C 2012 IrSr2Sm1.15Ce0.85Cu2.175O10: a reentrant spin-glass material *Phys. Rev.* B **85** 144419
[31] Grzechnik A, Kaindl R and Friese K 2007 Temperature dependent study of the crystal structure of NaCdZn2F7 pyrochlore *J. Phys. Chem. Solids* **68** 382–8
[32] Mydosh J A 2015 Spin glasses: redux: an updated experimental/materials survey *Reports Prog. Phys.* **78** 052501
[33] Bhatt R N and Lee P A 1982 Scaling studies of highly disordered spin-½ antiferromagnetic systems *Phys. Rev. Lett.* **48** 344–7
[34] Kimchi I, Sheckelton J P, McQueen T M and Lee P A 2018 Scaling and data collapse from local moments in frustrated disordered quantum spin systems *Nat. Commun.* **9** 4367
[35] Kimchi I, Nahum A and Senthil T 2018 Valence bonds in random quantum magnets: theory and application to YbMgGaO *Phys. Rev. X* **8** 031028
[36] Ramirez A P, Hessen B and Winklemann M 2000 Entropy balance and evidence for local spin singlets in a kagomé-like magnet *Phys. Rev. Lett.* **84** 2957–60
[37] Sindzingre P, Misguich G, Lhuillier C, Bernu B, Pierre L, Waldtmann C and Everts H-U 2000 Magnetothermodynamics of the Spin- 1/2 kagomé antiferromagnet *Phys. Rev. Lett.* **84** 2953–6
[38] Silverstein H J *et al* 2014 Liquidlike correlations in single-crystalline Y2Mo2O7 : an unconventional spin glass *Phys. Rev.* B **89** 054433
[39] Derzhko O, Hutak T, Krokhmalskii T, Schnack J and Richter J 2020 Adapting planck's route to investigate the thermodynamics of the spin-half pyrochlore heisenberg antiferromagnet *Phys. Rev.* B **101** 174426
[40] Sidey V 2017 Predicting the lattice parameters for the AIAIIBII2F7 disordered cubic fluoride pyrochlores *Zeitschrift fur Krist. - Cryst. Mater.* **232** 729–31
[41] Shannon R D 1976 Revised effective ionic radii and systematic studies of interatomic distances in halides and chalcogenides *Acta Crystallogr. Sect.* A **32** 751–67
[42] Abragam A and Pryce M H L 1951 The theory of paramagnetic resonance in hydrated cobalt salts *Proc. R. Soc. London. Ser. A. Math. Phys. Sci.* **206** 173–91
[43] Buyers W J L, Holden T M, Svensson E C, Cowley R A and Hutchings M T 1971 Excitations in KCoF 3: II. Theoretical *J. Phys. C: Solid State Phys.* **4** 2139–59
[44] Zheng W-C and Wu S-Y 2001 Explanation of the EPR g factors for Co^{2+} impurities in trigonal Cd2P2S6 crystal *Phys. B Condens. Matter* **307** 28
[45] Wang Y, Rosenbaum T F, Prabhakaran D, Boothroyd A T and Feng Y 2020 Approaching the quantum critical point in a highly correlated all-in-all-out antiferromagnet *Phys. Rev.* B **101** 220404
[46] Klicpera M, Vlášková K and Diviš M 2020 Characterization and magnetic properties of heavy rare-Earth A2Ir2O7 pyrochlore iridates, the case of Tm2Ir2O7 *J. Phys. Chem.* C **124** 20367–76
[47] Vlášková K, Proschek P, Diviš M, Le D, Colman R H and Klicpera M 2020 Magnetic properties and crystal field splitting of the rare-Earth pyrochlore Er2Ir2 O7 *Phys. Rev.* B **102** 054428
[48] Müller P, Lohmann A, Richter J and Derzhko O 2019 Thermodynamics of the pyrochlore-lattice quantum Heisenberg antiferromagnet *Phys. Rev.* B **100** 024424
[49] Bramwell S T and Harris M J 1998 Frustration in Ising-type spin models on the pyrochlore lattice *J. Phys. Condens. Matter* **10** L215
[50] Wong A W C, Hao Z and Gingras M J P 2013 Ground state phase diagram of generic XY pyrochlore magnets with quantum fluctuations *Phys. Rev. B - Condens. Matter Mater. Phys.* **88** 144402
[51] Zeisner J *et al* 2019 Magnetic interactions and spin dynamics in the bond-disordered pyrochlore fluoride NaCaCo2F7 *Phys. Rev.* B **99** 155104
[52] Frandsen B A, Ross K A, Krizan J W, Nilsen G J, Wildes A R, Cava R J and Birgeneau R J 2017 Real-space investigation of short-range magnetic correlations in fluoride pyrochlores NaCaCo2F7 and NaSrCo2F7 with magnetic pair distribution function analysis *Phys. Rev. Mater.* **1** 074412
[53] Ramirez A P 1994 Strongly geometrically frustrated magnets *Annu. Rev. Mater. Sci.* **24** 453–80